ARTICLE

Geometrical Doping at the Atomic Scale in Oxide Quantum Materials

Minsu Choi, Hyunwoo Jeon, Kitae Eom, Jinsol Seo, Seulki Roh, Ilwan Seo, Sang Ho Oh,
Jungseek Hwang, Yunsang Lee, Warren E. Pickett, Christos Panagopoulos, Chang-Beom Eom,
and Jaichan Lee*

Cite This: ACS Nano 2023, 17, 14814−14821

Read Online

ACCESS | Metrics & More | Article Recommendations | SI Supporting Information

ABSTRACT: Chemical dopants enabling a plethora of emergent physical properties have been treated as randomly and uniformly distributed in the frame of a three-dimensional doped system. However, in nanostructured architectures, the location of dopants relative to the interface or boundary can greatly influence device performance. This observation suggests that chemical dopants need to be considered as discrete defects, meaning that geometric control of chemical dopants becomes a critical aspect as the physical size of materials scales down into the nanotechnology regime. Here we show that geometrical control of dopants at the atomic scale is another fundamental parameter in chemical doping, extending beyond the kind and

amount of dopants conventionally used. The geometrical control of dopants extends the class of geometrically controlled structures into an unexplored dimensionality, between 2D and 3D. It is well understood that in the middle of the progressive dimensionality change from 3D to 2D, the electronic state of doped SrTiO$_3$ is altered from a highly symmetric charged fluid to a charge disproportionated insulating state. Our results introduce a geometrical control of dopants, namely, geometrical doping, as another axis to provide a variety of emergent electronic states via tuning of the electronic properties of the solid state.

KEYWORDS: chemical doping, atomic scale, oxide, metal−insulator transition, SrTiO$_3$
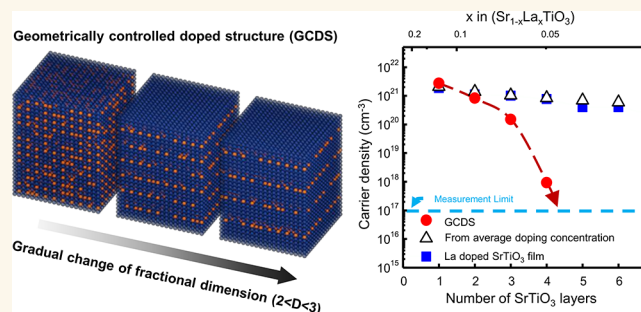
Chemical doping is a primary way to provide a material with charge carriers whose character, either extended or localized, is a cornerstone for further developing an immense variety of physical phenomena and material properties.[1] The extended solid-state family of materials subjected to chemical doping includes semiconductors of p or n type, dielectrics that can be divided into high-k or ferroelectric polarization, high-T$_c$ superconductors, and magnetic systems with itinerant or localized electrons.[2] Chemical doping has been treated in a random and uniform distribution, i.e., nonlocal effect, on a micrometer scale. However, chemical dopants need to be treated as discrete defects as the length scale of the interdistance between the dopants becomes similar to the feature length scale of a given property,[3,4] or a device scale such as channel length in a semiconductor,[5−8] where quantum effects begin to appear prominently. Device performance, for example threshold voltage in a Si semiconductor, has been shown to be influenced by the location of discrete defects relative to source and drain in the device.[9,10] Therefore, the geometric distribution of dopants in a feature scale of nanostructured materials, perhaps determining the dimension-

ality of a doped material, can be another fundamental parameter that provides yet enriched functionalities in emergent technologies in addition to the kinds and amounts of chemical dopants that have been used conventionally.

We introduce the geometrical control of dopants, namely geometrical doping, a further dimension in the engineering of nanostructures, in transition-metal oxides (TMOs) to tune the fundamental properties of material architectures. In a TMO featured by the partial occupancy of d orbitals and the collective interplay between the internal degrees of freedom (charge, spin, orbital, and lattice), chemical doping leads to a succession of electronic or quantum states, for example, from insulator to metal, from antiferromagnetic to ferromagnetic or
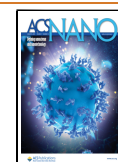
no magnetic order, and occasionally from insulator to superconductor, displaying substantial changes in their properties.[11,12] Notably, external perturbations such as electric field, magnetic field, light, and pressure[13−18] providing material tunability are already utilized in solid-state electronics.[19,20] In this study, the geometrical aspect of the dopants was added to the tuning parameters toward a further fundamental understanding and enrichment of properties of a TMO.

Among the wide variety of geometries of dopant distribution, the two-dimensional confinement of dopants was used in this work. In other words, the dopant distribution is confined only to an atomic plane, and thus one geometrical axis of the random distribution of the dopants is eliminated. In the geometrically controlled doped structure (GCDS), the anisotropy between dopants may be reflected as a gradual variation of the dimensionality of chemical doping (Figure 1) within the Thomas−Fermi screening length scale of the material studied. This leads to a gradual change in the state of the GCDS between 2D and 3D and drives the system across the metal−insulator transition (MIT) even at a fixed dopant
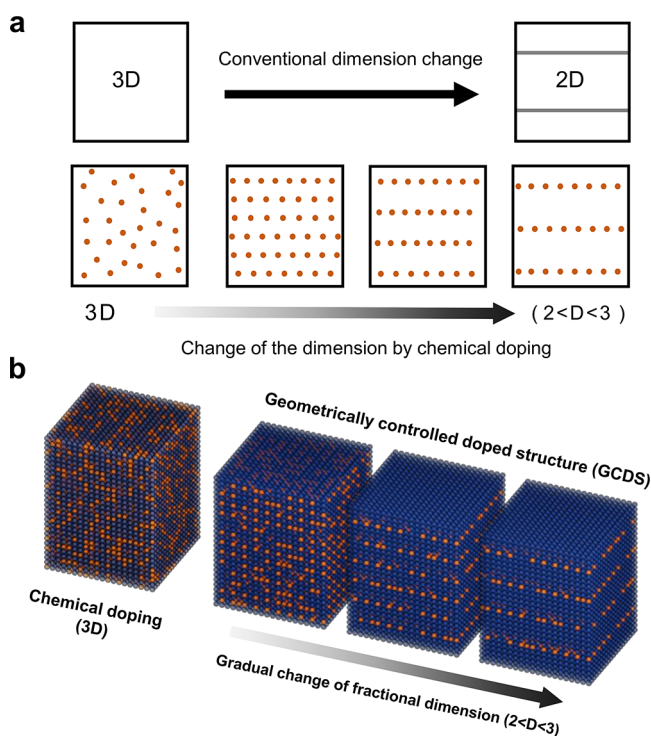
concentration, offering another way to prompt and tune an emerging electronic phase. By controlling the geometrical distribution of chemical dopants, we demonstrate the span of the state of matter from a charge fluid to a disproportionated state in the middle of the gradual change from 3D to 2D, offering another "dimension" for engineering chemical doping.

Doping in a geometrically controlled manner is achieved by the periodic insertion of a doped monolayer TMO into an undoped parent compound over a varying period. The chemically doped layer employed here was 25% La-doped $SrTiO_3$ (SLTO), far below the critical point (95% La) required for electron half-filling in a bulk state.[21,22] The Thomas−Fermi screening length of 25% La-doped $SrTiO_3$ ranges from 1 to 3 unit cell (uc) distances. Figure 1b shows that the dimensionality (D) of GCDS varies as a function of the period, i.e., the thickness of the parent compound (n). For example, GCDS with n = 1 uc (second panel from the left in Figure 1b) has La defects at a distance of 2 uc along the z direction. This resembles a 3D randomly doped structure (first panel on the left in Figure 1b), since on average the distance between La defects in 25% SLTO is 1.6 uc. With an increase in n, the distance between La dopants along the z direction increases, and accordingly, the dimensionality of GCDS is lowered progressively from 3D (see the lower panel in Figure 1b) in a fractional manner. However, GCDS for high n is distinguished from 2D, for example, $LaTiO_3$/$SrTiO_3$ (LTO/STO) superlattices since LTO/STO superlattices are always a 2D structure regardless of the thickness of the STO layer (compare the right panel in the upper and lower panels in Figure 1a). Another criterion for the distinction between GCDS and a superlattice is the presence/absence of the interface considering La dopants as the discrete defects in a bulk host material. GCDS has no interface at all, whereas superlattices have an interface with 2D properties. Therefore, GCDS with variable n is distinct from 3D or 2D since the dimensionality varies between 2D and 3D, whereas the material dimensionality has been considered within an integral number such as 1D, 2D, and 3D. The classes of solid-state materials become extended beyond conventionally reported classes by the geometrical control of dopants at the atomic scale.

The gradual variation in GCDS dimensionality is possible due to the precise control of the atomic layer thickness in our structures. GCDS with n = 1−5 were grown by pulsed-laser deposition on TiO_2-terminated (001)-oriented STO substrates using the growth conditions discussed earlier.[23] Ambient oxygen with ozone was used to ensure oxygen stoichiometry in the GCDSs (Figure S1). The thickness of each STO and SLTO layer was controlled to within 1 uc by monitoring the *in situ* reflection high-energy electron diffraction (RHEED) growth oscillations (Figure S2a). Atomic force microscopy (AFM) images show atomically flat surfaces, preserving the step-terrace structure of the STO substrate (inset of Figure S2a).

Figure 1. Concept of geometrically controlled doped structure. (a) Schematic dimensional change of a geometrical structure. The orange sphere represents a discrete point (for example, a dopant atom). The geometric structure with random distribution of dopants is in a 3D state (left). By confining the distribution of dopants in a 2D way and increasing the distance between the confined layers, the geometric structure gradually changes to a low-dimensional state and becomes similar to a 2D structure (right). (b) Schematic dimensional change of La-doped $SrTiO_3$ to a geometrically controlled doped structure (GCDS). La defects (orange) are confined in a 2D atomic layer while the thickness of undoped $SrTiO_3$ (n) is varied. The bulk SLTO has a random distribution of La dopants and is in a 3D state. In GCDS with n = 1 (second panel from the left in (b)), the distribution of defects is similar to that of a 3D chemical doped state. In GCDS with n = 5 (right panel in (b)), the anisotropy in the distance of La defects renders GCDS close to a 2D state.

RESULTS AND DISCUSSION

Electron Localization in Geometrically Controlled Doped Structures. Figure 2a shows atomic resolution energy-dispersive X-ray spectroscopy (EDS) maps of Ti, Sr, La, and O in GCDS with n = 5. The EDS maps reveal that the distribution of La dopants along [001] is highly concentrated to 1 uc next to the doped atomic layer. The La atom profile measured by EELS along [001] also confirms the geometric
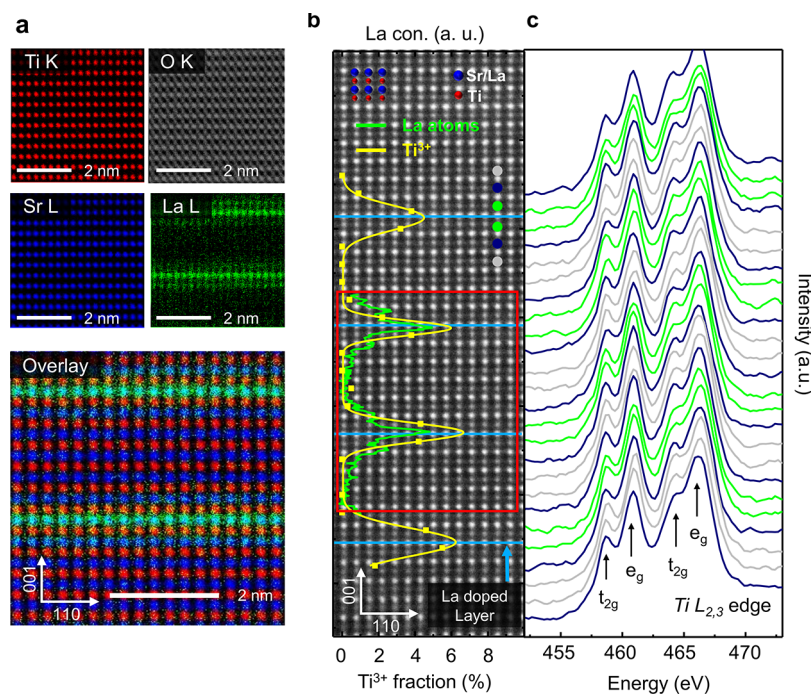
Figure 2. Element and charge distributions in geometrically controlled doped structure (GCDS). (a) Atomic resolution EDS maps of GCDS with $n = 5$ obtained along the $\langle 110 \rangle$ zone axis. (b) High-angle annular dark field (HAADF) STEM images of GCDS with lattice coherence. The positions of Sr/La (blue) and Ti (red) columns are highlighted in the inset. The green and yellow lines represent the concentration profile of La determined by EDS elemental mapping and the fraction of Ti^{3+} determined by multiple linear least-squares fitting of atomic layer resolved EELS Ti-$L_{2,3}$ line profiles, respectively. (c) Line profile of the EELS Ti $L_{2,3}$ edge obtained across the La-doped $SrTiO_3$ layers shown in (b). The green lines represent the TiO_2 layers nearest to the La-doped SrO layer. The reference EELS Ti $L_{2,3}$ edge of Ti^{3+} in $LaTiO_3$ has a broad maximum between t_{2g} and e_g peaks of Ti^{4+} in $SrTiO_3$, leading to broadening of the spectrum when Ti has a mixed valence state between Ti^{4+} and Ti^{3+}. Reference spectra for Ti^{4+} and Ti^{3+} are also shown in Supplementary Note 2, taken from $SrTiO_3$ and $LaTiO_3$ films, respectively.

control of dopants at the atomic scale (Figure 2b). X-ray diffraction studies, including symmetric Bragg scans and reciprocal space maps (RSM), revealed reflections from the periodic arrangement of dopants in the out-of-plane direction, corresponding to each GCDS (Supplementary Note 1). The presence of thickness fringes arising from the central Bragg peak ($GCDS_{(0)}$ [002]) and satellite ($GCDS_{(-1)}$ [002] and $GCDS_{(+1)}$ [002]) peaks adds credence to the high quality of the samples and well-defined periodicity (Figure S2b). RSM for GCDS indicated that the samples were grown epitaxially along [001] without strain relaxation (Figure S2c). Following the confinement of La atoms in a 2D way at the atomic scale, importantly the STEM EELS Ti-$L_{2,3}$ edge for GCDS with $n = 5$ indicated that the presence of Ti^{3+} due to La doping was confined next to the La-doped layer (Figure 2b,c). This behavior is distinct from SLTO bulk doping in a random 3D way, where charge transfer from La dopants becomes confined and localized to within 1 uc of the La-doped layer in GCDS, whereas excess charges from La dopants are well extended in SLTO bulk doping.

Electrical and Optical Transport of Geometrically Controlled Doped Structures. The outcome of confining dopants is the change in the character of charge carriers generated by La doping, evident in the DC and optical transport behaviors of GCDS with an increase in n. Figure 3a depicts a MIT with increasing n. A metallic phase is observed for $n = 1$ and 2, whereas for $n = 3$ GCDS remains conducting down to $T = 45$ K, with a slight upturn in $R(T)$ foreshadowing an insulating state at lower temperature. Fermi-liquid-like

behavior $\rho \approx AT^2$ with increasing residual resistivity is observed for $n = 1$, 2, and 3 (Figure S3), in agreement with bulk SLTO.[21,22] A rapid increase in coefficient A (electron−electron interaction) is observed with increasing n (or decreasing dimensionality). For $n \geq 4$, GCDS becomes an insulator, indicative of MIT as we move from 3D to 2D.

The carrier densities of GCDS determined from transport measurements were compared with the estimates from the nominal average La doping concentration (from 12.5% to 3.7% for GCDS with $n = 1−5$) and the experimental values of SLTO single-layer films and single crystals (Figure 3b and Figure S4).[21,22] The experimentally determined carrier density for $n = 1$ is similar to that of an SLTO single-layer film and single crystal, whereas the carrier density for $n = 2$ is reduced by a factor of 2, compared to bulk SLTO (single-layer film and single crystal). A larger discrepancy, however, emerged at $n = 3$ with the onset of a MIT. The carrier density for $n \geq 3$ drops rapidly compared with the measured values of SLTO single-layer films with the same average La concentration of GCDS or the mean value estimated from the average nominal La concentration. Therefore, note that this electronic transition is not caused by low carrier densities due to the dilution of extended electrons throughout GCDS. Instead, charge localization occurs as a consequence of the confined distribution of dopants. As n increases, charge localization and transfer are increasingly confined at the $Ti−O_2$ layer adjacent to the La-doped layer, leading to Ti^{3+} (Figure 2b,c).

The observed magnetoresistance (MR) shows signatures of electron localization and relevant electronic states for $n \geq 3$
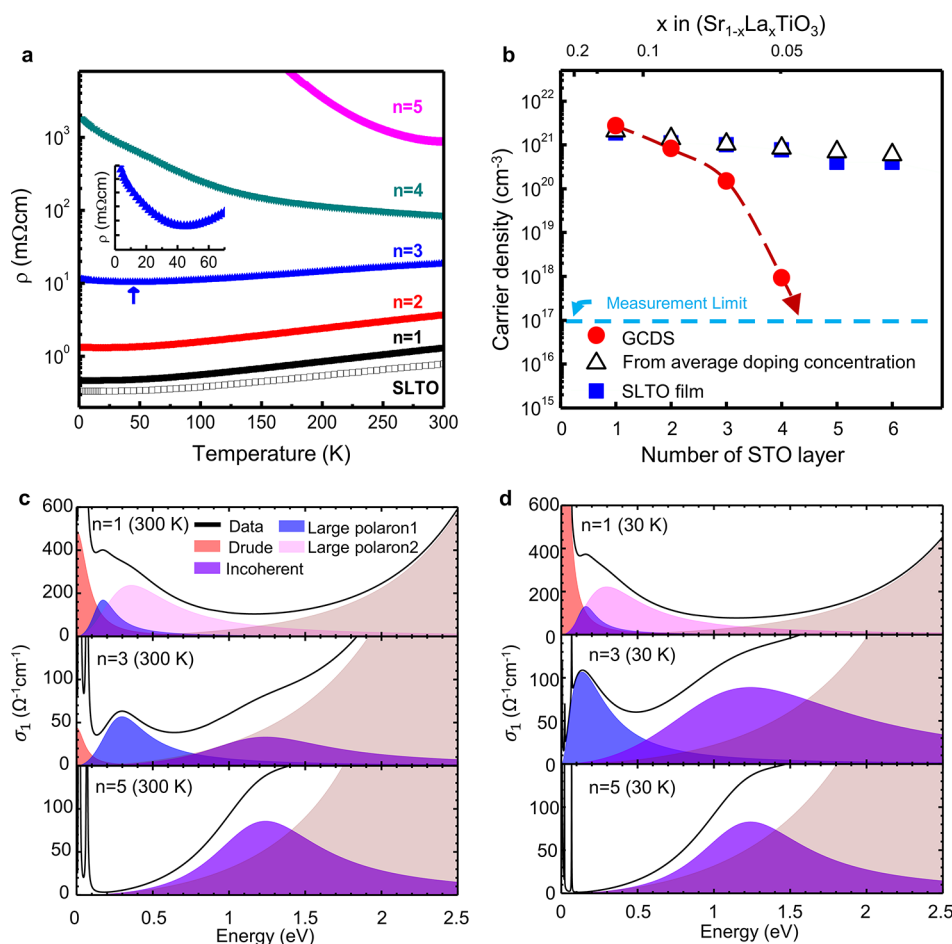
Figure 3. Transport properties of geometrically controlled doped structure. (a) Temperature dependence of resistivity. The inset shows a low-temperature region for GCDS with $n = 3$ and upturn at ~45 K. (b) Variation in carrier density as a function of the number of STO layers (n). The carrier densities of GCDSs are compared with those estimated from the average La doping concentration and obtained from Hall effect measurements of SLTO single-layer films at room temperature. (c, d) Optical conductivity of GCDS measured at 30 K and room temperature. The spectral weight of the coherent component is transferred gradually to an incoherent portion as n increases. Drude and polaron modes are distinctive in the absence of incoherent mode at $n = 1$. Large polaron modes in the MIR range are identified by comparing with the Nb-doped STO.[33] For $n = 3$, the Drude mode disappears at 30 K below the MIT temperature (50 K) while an incoherent mode appears. Only the incoherent mode is observed at $n = 5$, which is consistent with DC transport results.

(Figure S5). For $n < 3$, we observed positive MR, consistent with metallic, nonmagnetic bulk SLTO. The positive MR increases with n, indicating the increase in the electron−electron interaction, and is saturated at high magnetic fields for $n = 3$, unlike bulk SLTO. The "M" shape and isotropic MR are acquired with a resistance reduction of −6% at 9 T for $n = 4$ (Figure S5) since a large negative MR due to the generation of a spin state caused by the electron localization on Ti and subsequent response of an antiparallel spin state at high magnetic fields is added to the positive MR.[24−26] These results show the change of character of the electronic transport by increasing the number of STO layers. This localization feature in GCDS with high n is quite different from SrTiO$_3$ with an intervening LaTiO$_3$ layer, i.e., LaTiO$_3$/SrTiO$_3$ superlattices with 2D electron gas[27] and δ-doped SrTiO$_3$ structures with a Nb-doped layer.[4]

Figures 3c,d depicts the optical conductivity spectra $\sigma_1(\omega)$, characteristic of conduction electrons (coherent mode) and localized electrons (incoherent mode), corresponding to Drude and Lorentz modes in the mid-infrared (MIR) range and near 1.3 eV, respectively (Figures S6 and S7). In the metallic state at low n, the Drude model from the coherent

mode dominates, which is characteristic of doped semi-conductors. A peak in MIR range, typical for electron-doped STO, is attributed to large polarons.[28] The spectral weight (SW) transfer in the Drude model with increasing n is consistent with the DC transport results, as depicted in Figures 3a,b and Figures S3 and S8. Simultaneously, the localized mode at ~1.3 eV from incoherent scattering emerges at $n = 3$ and becomes prominent at high n (Figure 3c). Notably, the incoherent part observed in GCDS is absent in the STO substrate and the 100 nm thick SLTO film (Figure S7). Therefore, defects cannot be the origin of the localized states. The optical feature of the localized mode in the insulating GCDS is reminiscent of electron localization caused by electron−electron interaction, i.e., the Mott state, in 3d transition-metal oxides. Additionally, electron−lattice coupling could give an additional contribution to the incoherent SW.[29] The polaronic effective mass (m^*_{pol}) was estimated from the coherent and large polaron SW shown in Figure 3c. Similar to the increase in m^*_{pol} from 3D to 2D owing to electron−lattice coupling,[30,31] the polaronic effective mass is enhanced from 4.96 to 9.00 as n changes from 1 to 3 (see Supplementary Note 3 for details), concomitant with the metal−insulator transition
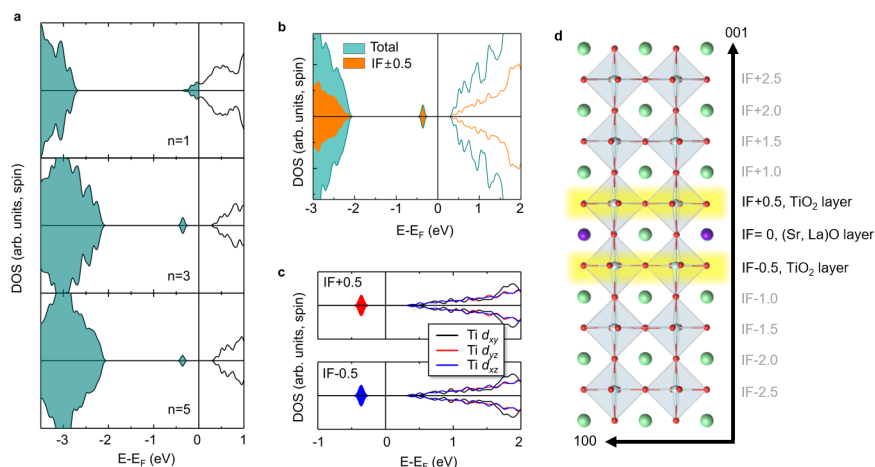
Figure 4. Electronic density of states of geometrically controlled doped structures. (a) Total density of states (DOS), showing the evolution from a metal to an insulating state with increasing n from 1 to 5. (b) Total and layer-resolved DOS for $n = 5$, showing that electrons from the doped layer are primarily localized in the TiO_2 layers (IF $\pm$ 0.5) next to the La-doped layer (IF). (c) Layer-resolved projected DOS of Ti ions along a Ti column at IF $\pm$ 0.5 for $n = 5$, showing that the localized states are occupied at Ti, resulting in charge disproportionation. d_{yz} and d_{xz} are preferentially occupied in IF + 0.5 and IF − 0.5, respectively. (d) Atomic layer for GCDS with $n = 5$ near the doped (Sr,La)O atomic layers. Each atom is designated in purple (La), green (Sr), cyan (Ti), and red (O).

by geometrically confining the dopants, which can be compared with SLTO bulk doping ($m^*_{pol} = 4.2$).[32]

First-Principles Calculation. Density-functional-theory (DFT) calculations within the DFT+U approach were performed to study the electronic states of GCDS. Figure 4a shows the total density of states (DOS) of GCDS for $n = 1$, 3, and 5. For $n = 1$, the doped electrons occupy states in the STO conduction band similar to bulk SLTO, resulting in a 3D electron gas. Only the paramagnetic metallic phase is stable, and all Ti sites have the same mean formal valence. For $n = 3$ and 5, doped electrons occupy a localized state in the STO band gap, showing insulating behavior. An earlier first-principles calculation suggested the progressive restriction of electron transfer along the z direction with increasing n.[33] Further, the insulating state emerges at high n when the Hubbard U parameter is above 3.7 eV, a range that is consistent with previous studies of titanates. While the Coulomb on-site electron–electron repulsion has been treated by a Hubbard repulsion U, polaron hopping in a distorted lattice can be modeled by the Hubbard U viewpoint.[34] Despite the low concentration of La dopant (25%) far from the critical point (95%), the onset of MIT occurs from the simultaneous enhancement of electron–electron correlation and electron–lattice coupling and associated localization, observed in DC transport and optical conductivity with increasing n.

DFT calculations show that electron localization occurs in the layers next to the doped layers. The total and layer-resolved DOSs for $n = 5$ (Figure 4b and Figure S9) show that the localized electrons corresponding to Ti^{3+} sites primarily occupy TiO_2 layers (IF + 0.5 and IF − 0.5) next to the doped (Sr,La)O atomic layers (IF), which is observed in the atomic layer resolved STEM EELS data (Figure 2b,c). Furthermore, the layer-resolved projected DOS of the Ti ions along the Ti column (Figure 4c) indicates that the d_{yz} orbital is split from the other t_{2g} orbitals and is primarily occupied at the TiO_2 layer (IF + 0.5). The localized states on Ti^{3+} are diagonally separated at the same layer (IF + 0.5) shown in Figure 4d and Figure S10a. Similarly, orbital splitting and occupation into d_{xz} occur at the layer (IF − 0.5). This symmetry-breaking of the tetragonal (d_{xz}, d_{yz}) equivalence indicates orbital ordering in

the crystal field split-off doublet within TiO_2 layers but also mirror-symmetry breaking across the dopant layer. The orbital degeneracy-breaking of GCDS was experimentally verified by X-ray linear dichroism (Figure S11 and Supplementary Note 4). Preferential orbital occupation in Ti develops into out-of-plane (d_{xz}, d_{yz}) orbitals as n increases from 1 to 5, consistent with the DFT results.

The evolution of MIT and the emerging electronic state could be attributed to numerous broken symmetries from the results of DFT calculations. The orbital splitting is further represented by simultaneous octahedral rotation and Jahn–Teller Q_2 mode like distortion at the doped layer (Figure S12). Note that the layer with localized electrons seems to be a combined rotation of the nearest doped $SrTiO_3$ ($a^0a^0c^-$) layer and 25% La doped bulk $SrTiO_3$ ($a^-a^-c^0$), which is not the same as any of $SrTiO_3$, 25% La-doped bulk $SrTiO_3$ and $LaTiO_3$ ($a^-a^-c^+$).[35] This insulating state is charge, orbital, and antiferromagnetic (AFM) spin ordered (Figure S10), close to the other members of the $R^{3+}TiO_3$ family, which have more electron and lattice distortion depending on the size of the A-site cation.[12] The accompanying mirror-symmetry breaking also breaks the inversion symmetry: a Mott insulating charge, spin, orbital, and inversion symmetry breaking down to the most primitive symmetry, one step beyond the "massive symmetry breaking" of the nonlayer-doped (111) LTO/STO interface.[36] The resulting physical properties are, of course, far from bulk doped STO systems. Emerging phases are induced by the simultaneous enhancement of electron–electron and electron–lattice couplings in the middle of the transformation in electronic dimensionality, which occurs far from the onset of the critical phenomena of bulk doped STO systems.

CONCLUSIONS

We have reported here another "dimension" (axis) to tune material properties by the geometrical confinement of dopants. Geometrical control of dopants at the atomic scale is another fundamental parameter in chemical doping, in addition to the kind and amounts of dopants conventionally used. The geometrical control of dopants alters the character of the charge carriers, providing the initial means for further

developing an immense variety of physical properties and enabling the tunability of electronic states of charge, spin, orbital, and lattice degrees of freedom. The geometrical aspects of dopants can be extended to solid-state materials, including semiconductors to superconductors, of not only 3D but also 2D properties with certain geometries of dopant or adatom distribution. This approach provides insights beyond conventional methods for tuning by controlling the kind and amount of a chemical dopant, ultimately for designing distinctive nanostructured materials with various functionalities.

METHODS AND EXPERIMENTAL DETAILS

Synthesis of Geometrically Controlled Doped Structures. Geometrically controlled doped structures (GCDS) were grown by pulsed laser deposition (PLD) on TiO_2-terminated $SrTiO_3$ (STO) substrates buffered with 10 unit cells (uc) of STO. A KrF excimer laser (248 nm) beam was focused on the $SrTiO_3$ single crystal and 25% La-doped $SrTiO_3$ (SLTO) target to an energy density of ∼1.2 J cm^{-2} and pulsed at 2 Hz. GCDS were grown at a substrate temperature of 650 °C and $P_{O_2} = 1 \times 10^{-5}$ Torr. In order to examine the absence of additional electrons caused by the oxygen vacancies, SLTO films (100 nm) were grown at oxygen pressures varying from 2×10^{-7} to 1×10^{-5} Torr and a fixed growth temperature of 650 °C. During growth, an 8% ozone mixture in oxygen was used to facilitate the incorporation of oxygen in the films. The carrier density of SLTO films (Figure S1) saturates at oxygen pressures above 1×10^{-6} Torr and is comparable with single-crystal SLTO.[21] This indicated that the contribution of oxygen vacancies to the carriers is insignificant at the pressure used in this study, $P_{O_2} = 1 \times 10^{-5}$ Torr.

STEM−EELS and EDS Measurements. The specimens for scanning transmission electron microscopy (STEM) were prepared by using a triple-beam focused ion beam system (NX2000, Hitachi). The specimens were first thinned by using a Ga^+ ion beam at an acceleration voltage of 30 kV for electron beam transparency and then at 5 kV, followed by 1 kV, to reduce the surface damages. Finally, the TEM specimens were milled by using an Ar^+ ion beam at 1 kV in the same FIB system to further reduce the surface damage layers on both sides of the specimen. STEM imaging, energy dispersive X-ray spectroscopy (EDS), and electron energy loss spectroscopy (EELS) were carried out using a spherical aberration corrected microscope (JEM-ARM200F, JEOL) operated at 200 kV. The convergence angle for atomic-resolution STEM imaging and EDS elemental mapping was 32 mrad. The atomic-scale EDS mapping data of the sample were acquired by utilizing a dual-type EDS detector (an effective X-ray detection area of a 100 mm^2 for each) with a large effective solid angle (∼0.8 sr) and a highly focused electron probe (∼0.96 Å) at an electron-dose rate of 8.5×10^{10} electrons nm^{-2} s^{-1}. The resulting elemental maps were obtained by a multiple-frame summation up to 1500 frames with 256×256 pixel resolution and an acquisition time of 10 μs per pixel (maximum total acquisition time, ∼16.5 min). The background noise floor in each map was removed by applying a Wiener filter. The EELS data sets were obtained using an energy filter (Gatan GIF Quantum ER 965, USA). The energy resolution of the EELS spectrum was estimated to be 0.6 eV from the full width at half-maximum of the zero loss peak.

Electrical Transport Measurements. Electrical characterization of GCDS with temperature was obtained by using a Physical Properties Measurement System (PPMS, Quantum Design Inc.). Hall bars were patterned by lithography and etching processes. Au/Pt metal contacts were deposited by e-beam evaporation on the sides of each bridge of the Hall bar patterns. Pt wires were bonded to the metal contacts for electrical wiring to PPMS. The carrier density of each sample was determined by $n = I/((dV_H/dB) \times t \times q)$, respectively (Figure 3b and Figure S5). I, V_H, t, B, and q represent electric current, Hall voltage, film thickness, magnetic field applied perpendicular to the plane of the samples, and electric charge, respectively.

Optical Conductivity Measurements. The complex optical conductivity spectra were obtained by using two different spectrometers. For a spectral range of 0.006−3.1 eV, we used a Bruker Vertex 80v FTIR spectrometer with a liquid He cryostat to obtain temperature-dependent reflectance spectra. A PerkinElmer Lambda 950 monochromatic spectrometer was used for a spectral range from MIR to UV (0.6−6.2 eV) at room temperature. An *in situ* Au-evaporation technique was applied to obtain accurate reflectance spectra.[37] The measured reflectance spectra of the GCDS ($n = 1, 3$, and 5) samples and bare STO substrate at various temperatures between 30 and 300 K are shown in Figure S6a−d.

First-Principles Calculation. Density functional theory calculations were performed within the Perdew−Burke−Ernzerhof generalized gradient approximation (GGA-PBE) as implemented in the Vienna *ab* initio simulation package (VASP).[38,39] The projector augmented wave (PAW) method with a kinetic energy cutoff of 400 eV for the plane wave basis set was used.[40,41] Electronic correlations were treated within the rotationally invariant LSDA+U approach of Liechtenstein et al.[42] To fit the experimental results, we assumed ($U−J$) = 5−0.64 eV for Ti 3d orbitals, while for La 4f orbitals, ($U−J$) was assumed to be 11−0.68 eV to avoid spurious mixing with the STO conduction band. Three GCDS configurations with $n = 1, 3, 5$ were modeled into supercells consisting of $4 \times 4 \times m$ (m = 2, 4, 6) ucs with the antiferrodistortive tetragonal phase, respectively.

These large supercells allowed us to study possible charge, spin, and orbital orderings. Correspondingly, $3 \times 3 \times p$ ($p = 6, 3, 2$) Monkhorst $\vec{k}$-point grids were used to sample the Brillouin zones for the supercells $4 \times 4 \times m$ (m = 2, 4, 6), respectively. A Gaussian smearing method with a smearing width $\sigma = 0.05$ eV was used for all of the calculations. In the doped layer, 4 out of 16 Sr atoms were substituted by La atoms. The in-plane lattice constants were constrained at the calculation-optimized value of bulk STO. All atoms were fully relaxed with atomic forces <|0.01| eV/Å.

X-ray Linear Dichroism. To investigate an orbital structure of Ti atoms in GCDS, we performed polarization-dependent Ti $L_{2,3}$ X-ray absorption spectroscopy (XAS) measurements. The in-plane (d_{xy}) and out-of-plane (d_{xz} and d_{yz}) Ti orbitals were probed by aligning linearly polarized light along the directions perpendicular and parallel to the film surface, resulting in XAS spectra with in-plane (I_{ab}) and out-of-plane (I_c) intensities. From these spectra, the anisotropic orbital distribution can be estimated by the X-ray linear dichroism (XLD) intensity obtained by subtracting I_{ab} from I_c in the XAS data.[43] The XAS spectra were obtained by total electron yield mode, and the polarized beam was aligned by a 23° angle to the sample surface. All spectroscopic experiments were carried out at the 2A beamlines of the Pohang Accelerator Laboratory (PAL).

ASSOCIATED CONTENT

ⓢ Supporting Information

The Supporting Information is available free of charge at https://pubs.acs.org/doi/10.1021/acsnano.3c03038.

> Carrier density with an ambient oxygen pressure in the growth of $Sr_{0.75}La_{0.25}TiO_3$ films, *in situ* RHEED and *ex situ* characterizations of GCDS, transport behavior in GCDS, carrier density vs La content, magnetoresistance in GCDS, reflectance of GCDS and substrate, the film-fit, optical conductivity of GCDS and SLTO thin film and STO substrate, DC resistivity obtained from the optical conductivity, layer-resolved density of state (DOS) of GCDS, orbital structure of GCDS, lattice distortion in GCDS, charge disproportionation, and orbital and spin ordered state of GCDS (PDF)

AUTHOR INFORMATION

Corresponding Author

Jaichan Lee − *School of Advanced Materials Science and Engineering, Sungkyunkwan University, Suwon 16419,*

Republic of Korea; CompAID Research, Suwon 16419, Republic of Korea; ● orcid.org/0000-0002-2730-9492; Email: jclee@skku.edu

Authors

Minsu Choi − *School of Advanced Materials Science and Engineering, Sungkyunkwan University, Suwon 16419, Republic of Korea; CompAID Research, Suwon 16419, Republic of Korea*

Hyunwoo Jeon − *School of Advanced Materials Science and Engineering, Sungkyunkwan University, Suwon 16419, Republic of Korea*

Kitae Eom − *School of Advanced Materials Science and Engineering, Sungkyunkwan University, Suwon 16419, Republic of Korea; Department of Materials Science and Engineering, University of Wisconsin−Madison, Madison, Wisconsin 53706, United States*

Jinsol Seo − *Department of Energy Engineering, Institute for Energy Materials and Devices, Korea Institute of Energy Technology (KENTECH), Naju 58330, Republic of Korea*

Seulki Roh − *Department of Physics, Sungkyunkwan University, Suwon 16419, Republic of Korea; ● orcid.org/0000-0003-0424-614X*

Ilwan Seo − *Department of Physics, Soongsil University, Seoul 06978, Republic of Korea*

Sang Ho Oh − *Department of Energy Engineering, Institute for Energy Materials and Devices, Korea Institute of Energy Technology (KENTECH), Naju 58330, Republic of Korea*

Jungseek Hwang − *Department of Physics, Sungkyunkwan University, Suwon 16419, Republic of Korea; ● orcid.org/0000-0002-2555-1218*

Yunsang Lee − *Department of Physics, Soongsil University, Seoul 06978, Republic of Korea*

Warren E. Pickett − *Department of Physics, University of California Davis, Davis, California 95616, United States*

Christos Panagopoulos − *Division of Physics & Applied Physics, School of Physical & Mathematical Sciences, Nanyang Technological University, Singapore 639798, Singapore*

Chang-Beom Eom − *Department of Materials Science and Engineering, University of Wisconsin−Madison, Madison, Wisconsin 53706, United States; ● orcid.org/0000-0002-8854-1439*

Complete contact information is available at:
https://pubs.acs.org/10.1021/acsnano.3c03038

Author Contributions

M.C. and J.L. conceived the project. M.C. and K.E. fabricated the thin films and performed the structural characterizations. M.C. and K.E. carried out electrical measurements. J.S. and S.H.O. performed STEM measurements. H.J. performed DFT calculations. M.C. and K.E. performed X-ray dichroism spectroscopy experiments. S.R. and J.H. performed optical reflectance measurements and analysis. I.S and Y.L. performed spectroscopic ellipsometry measurements. M.C., W.E.P., C.P., C.B.E., and J.L. interpreted the data and prepared the manuscript. J.L. supervised the study. All authors discussed the results and were involved in writing the manuscript.

Notes

The authors declare no competing financial interest.

REFERENCES

(1) Sze, S. M. *Physics of Semiconductor Devices*, 2nd ed.; Wiley: 1981.

(2) Chiang, Y.-M.; Birnie, D.; Kingery, W. D. *Physical Ceramics*; Wiley: 1997.

(3) Logvenov, G.; Gozar, A.; Bozovic, I. High-Temperature Superconductivity in a Single Copper-Oxygen Plane. *Science* **2009**, *326*, 699−702.

(4) Kozuka, Y.; Kim, M.; Ohta, H.; Hikita, Y.; Bell, C.; Hwang, H. Y. Enhancing the Electron Mobility via Delta-Doping in $SrTiO_3$. *Appl. Phys. Lett.* **2010**, *97*, No. 222115.

(5) Roy, S.; Asenov, A. Where Do the Dopants Go? *Science* **2005**, *309*, 388−390.

(6) Fuechsle, M.; Miwa, J. A.; Mahapatra, S.; Ryu, H.; Lee, S.; Warschkow, O.; Hollenberg, L. C.; Klimeck, G.; Simmons, M. Y. A Single-Atom Transistor. *Nat. Nanotechnol.* **2012**, *7*, 242−246.

(7) Koenraad, P. M.; Flatté, M. E. Single Dopants in Semiconductors. *Nat. Mater.* **2011**, *10*, 91−100.

(8) Prati, E.; Hori, M.; Guagliardo, F.; Ferrari, G.; Shinada, T. Anderson-Mott Transition in Arrays of a Few Dopant Atoms in a Silicon Transistor. *Nat. Nanotechnol.* **2012**, *7*, 443−447.

(9) Chiang, M.-H.; Lin, J.-N.; Kim, K.; Chuang, C.-T. Random dopant fluctuation in limited-width FinFET technologies. *IEEE Trans. Electron Devices* **2007**, *54*, 2055−2060.

(10) Choi, S.; Moon, D.; Kim, S.; Duarte, J.; Choi, Y. Sensitivity of threshold voltage to nanowire width variation in junctionless transistors. *IEEE Electron Device Lett.* **2011**, *32*, 125−127. (2011)

(11) Imada, M.; Fujimori, A.; Tokura, Y. Metal-insulator transitions. *Rev. Mod. Phys.* **1998**, *70*, 1039−1263.

(12) Tokura, Y.; Nagaosa, N. Orbital Physics in Transition-Metal Oxides. *Science* **2000**, *288*, 462−468.

(13) Fiebig, M.; Miyano, K.; Tomioka, Y.; Tokura, Y. Visualization of the Local Insulator-Metal Transition in $Pr_{0.7}Ca_{0.3}MnO_3$. *Science* **1998**, *280*, 1925−1928.

(14) Kiryukhin, V.; Casa, D.; Hill, J. P.; Keimer, B.; Vigliante, A.; Tomioka, Y.; Tokura, Y. An X-ray-Induced Insulator-Metal Transition in a Magnetoresistive Manganite. *Nature* **1997**, *386*, 813−815.

(15) Rata, A. D.; Herklotz, A.; Nenkov, K.; Schultz, L.; Dorr, K. Strain-Induced Insulator State and Giant Gauge Factor of $La_{0.7}Sr_{0.3}CoO_3$ Films. *Phys. Rev. Lett.* **2008**, *100*, 076401.

(16) Tokura, Y.; Kuwahara, H.; Moritomo, Y.; Tomioka, Y.; Asamitsu, A. Competing instabilities and metastable states in $(Nd,Sm)_{1/2}Sr_{1/2}MnO_3$. *Phys. Rev. Lett.* **1996**, *76*, 3184−3187.

(17) Caviglia, A. D.; Gariglio, S.; Reyren, N.; Jaccard, D.; Schneider, T.; Gabay, M.; Thiel, S.; Hammerl, G.; Mannhart, J.; Triscone, J.-M. Electric field control of the $LaAlO_3/SrTiO_3$ interface ground state. *Nature* **2008**, *456*, 624−627.

(18) Ueno, K.; Nakamura, S.; Shimotani, H.; Ohtomo, A.; Kimura, N.; Nojima, T.; Aoki, H.; Iwasa, Y.; Kawasaki, M. Electric field-induced superconductivity in an insulator. *Nat. Mater.* **2008**, *7*, 855−858.

(19) Goldman, A. M. Condensed Matter Physics: Magnetoresistance in layered Manganite Compounds. *Science* **1996**, *274*, 1630.

(20) Prinz, G. A. Magnetoelectronics. *Science* **1998**, *282*, 1660−1663.

(21) Tokura, Y.; Taguchi, Y.; Okada, Y.; Fujishima, Y.; Arima, T.; Kumagai, K.; Iye, Y. Filling dependence of electronic properties on the verge of metal−Mott-insulator transition in $Sr_{1-x}La_xTiO_3$. *Phys. Rev. Lett.* **1993**, *70*, 2126−2129.

(22) Okuda, T.; Nakanishi, K.; Miyasaka, S.; Tokura, Y. Large thermoelectric response of metallic perovskites: $Sr_{1-x}La_xTiO_3$ ($0 \le x \le 0.1$). *Phys. Rev. B* **2001**, *63*, No. 113104.

(23) Kim, J.; Kim, L.; Jung, D.; Lee, J. Growth of $SrTiO_3/(Sr_{1-x}La_x)TiO_3$ superlattices and lattice strain development. *Ferroelectrics* **2006**, *336*, 255−261.

(24) Preyer, N. W.; Kastner, M. A.; Chen, C. Y.; Birgeneau, R. J.; Hidaka, Y. Isotropic negative magnetoresistance in $La_{2-x}Sr_xCuO_{4+y}$. *Phys. Rev. B* **1991**, *44*, 407−410.

(25) Altshuler, B. L.; Aronov, A. G.; Lee, P. A. Interaction effects in disordered Fermi systems in two dimensions. *Phys. Rev. Lett.* **1980**, *44*, 1288−1291.

(26) Scherwitzl, R.; Gariglio, S.; Gabay, M.; Zubko, P.; Gibert, M.; Triscone, J.-M. Metal−insulator transition in ultrathin $LaNiO_3$ films. *Phys. Rev. Lett.* **2011**, *106*, No. 246403.

(27) Ohtomo, A.; Muller, D. A.; Grazul, J. L.; Hwang, H. Y. Artificial Charge-modulation in Atomic-scale Perovskite Titanate Superlattices. *Nature* **2002**, *419* (6905), 378−380.

(28) van Mechelen, J. L. M.; van der Marel, D.; Grimaldi, C.; Kuzmenko, A. B.; Armitage, N. P.; Reyren, N.; Hagemann, H.; Mazin, I. I. Electron-Phonon Interaction and Charge Carrier Mass Enhancement in $SrTiO_3$. *Phys. Rev. Lett.* **2008**, *100* (22), No. 226403.

(29) Basov, D. N.; Averitt, R. D.; van der Marel, D.; Dressel, M.; Haule, K. Electrodynamics of correlated electron materials. *Rev. Mod. Phys.* **2011**, *83* (2), 471−541.

(30) Peeters, F. M.; Wu, X.; Devreese, J. T. Exact and approximate results for the mass of a two-dimensional polaron. *Phys. Rev. B* **1988**, *37*, 933−936.

(31) Feynman, R. P. Slow electrons in a polar crystal. *Phys. Rev.* **1955**, *97*, 660−665.

(32) Moos, R.; Gnudi, A.; Härdtl, K. H. Thermopower of $Sr_{1-x}La_xTiO_3$ ceramics. *J. Appl. Phys.* **1995**, *78*, 5042−5047.

(33) Ong, P. V.; Lee, J.; Pickett, W. E. Tunable two-dimensional or three-dimensional electron gases by submonolayer La doping of $SrTiO_3$. *Phys. Rev. B* **2011**, *83*, No. 193106.

(34) Wang, Z.; Brock, C.; Matt, A.; Bevan, K. H. Implications of the DFT+U method on polaron properties in energy materials. *Phys. Rev. B* **2017**, *96*, No. 125150.

(35) Sunstrom, J. E.; Kauzlarich, S. M.; Klavins, P. Synthesis, structure, and properties of lanthanum strontium titanate $(La_{1-x}Sr_xTiO_3)$. *Chem. Mater.* **1992**, *4*, 346−353.

(36) Doennig, D.; Pickett, W. E.; Pentcheva, R. Massive Symmetry Breaking in $LaAlO_3/SrTiO_3(111)$ Quantum Wells: A Three-Orbital Strongly Correlated Generalization of Graphene. *Phys. Rev. Lett.* **2013**, *111*, No. 126804.

(37) Homes, C. C.; Reedyk, M.; Cradles, D. A.; Timusk, T. Technique for measuring the reflectance of irregular, submillimeter-sized samples. *Appl. Opt.* **1993**, *32*, 2976−2983.

(38) Perdew, J. P.; Burke, K.; Ernzerhof, M. Generalized Gradient Approximation Made Simple. *Phys. Rev. Lett.* **1996**, *77*, 3865−3868.

(39) Kresse, G.; Furthmüller, J. Efficient iterative schemes for ab initio total-energy calculations using a plane-wave basis set. *Phys. Rev. B* **1996**, *54*, 11169−11186.

(40) Blöchl, P. E. Projector augmented-wave method. *Phys. Rev. B* **1994**, *50*, 17953−17979.

(41) Kresse, G.; Joubert, J. From ultrasoft pseudopotentials to the projector augmented-wave method. *Phys. Rev. B* **1999**, *59*, 1758−1775.

(42) Liechtenstein, A. I.; Anisimov, V. I.; Zaanen, J. Density-functional theory and strong interactions: Orbital ordering in Mott-Hubbard insulators. *Phys. Rev. B* **1995**, *52*, R5467−R5470.

(43) Eom, K.; Choi, E.; Yoon, J.; Choi, M.; Song, K.; Choi, S. Y.; Lee, D.; Lee, J. W.; Eom, C. B.; Lee, J. Electron−Lattice Coupling in Correlated Materials of Low Electron Occupancy. *Nano Lett.* **2017**, *17*, 5458−5463.